

# Boron nitride substrates for high-quality graphene electronics

C. R. Dean<sup>1,2\*</sup>, A. F. Young<sup>3</sup>, I. Meric<sup>1</sup>, C. Lee<sup>4,5</sup>, L. Wang<sup>2</sup>, S. Sorgenfrei<sup>1</sup>, K. Watanabe<sup>6</sup>, T. Taniguchi<sup>6</sup>, P. Kim<sup>3</sup>, K. L. Shepard<sup>1</sup> and J. Hone<sup>2\*</sup>

**Graphene devices on standard SiO<sub>2</sub> substrates are highly disordered, exhibiting characteristics that are far inferior to the expected intrinsic properties of graphene<sup>1–12</sup>. Although suspending the graphene above the substrate leads to a substantial improvement in device quality<sup>13,14</sup>, this geometry imposes severe limitations on device architecture and functionality. There is a growing need, therefore, to identify dielectrics that allow a substrate-supported geometry while retaining the quality achieved with a suspended sample. Hexagonal boron nitride (h-BN) is an appealing substrate, because it has an atomically smooth surface that is relatively free of dangling bonds and charge traps. It also has a lattice constant similar to that of graphite, and has large optical phonon modes and a large electrical bandgap. Here we report the fabrication and characterization of high-quality exfoliated mono- and bilayer graphene devices on single-crystal h-BN substrates, by using a mechanical transfer process. Graphene devices on h-BN substrates have mobilities and carrier inhomogeneities that are almost an order of magnitude better than devices on SiO<sub>2</sub>. These devices also show reduced roughness, intrinsic doping and chemical reactivity. The ability to assemble crystalline layered materials in a controlled way permits the fabrication of graphene devices on other promising dielectrics<sup>15</sup> and allows for the realization of more complex graphene heterostructures.**

The quality of substrate-supported graphene devices has not improved since the first observation of the anomalous quantum Hall effect in graphene and its bilayer<sup>1–2</sup>. On SiO<sub>2</sub>, carrier mobility is limited by scattering from charged surface states and impurities<sup>3–6,8</sup>, substrate surface roughness<sup>9–11</sup> and SiO<sub>2</sub> surface optical phonons<sup>7,8</sup>. Moreover, near the Dirac point, substrate-induced disorder breaks up the 2D electron gas (2DES) into an inhomogeneous network of electron and hole puddles<sup>5,6,12</sup>, while charged impurities trapped in the substrate or at the graphene–substrate interface cause doping of the 2DES away from charge neutrality. So far, efforts to engineer alternatives to SiO<sub>2</sub> have typically involved other oxides, where similar surface effects continue to cause problems<sup>16–18</sup>.

Hexagonal boron nitride (h-BN) is an appealing substrate dielectric for use in improved graphene-based devices. h-BN is an insulating isomorph of graphite with boron and nitrogen atoms occupying the inequivalent A and B sublattices in the Bernal structure. The different on-site energies of the boron and nitrogen atoms result in a large (5.97 eV) bandgap<sup>19</sup> and a small (1.7%) lattice mismatch with graphite<sup>20</sup>. Owing to the strong, in-plane, ionic bonding of the planar hexagonal lattice structure, h-BN is relatively inert and is expected to be free of dangling bonds or surface charge traps. Furthermore, the

atomically planar surface should suppress rippling in graphene, which has been shown to mechanically conform to both corrugated and flat substrates<sup>9,21</sup>. The dielectric properties of h-BN ( $\epsilon \approx 3–4$  and  $V_{\text{breakdown}} \approx 0.7 \text{ V nm}^{-1}$ ) compare favourably with those of SiO<sub>2</sub>, allowing the use of h-BN as an alternative gate dielectric with no loss of functionality<sup>22</sup>. Moreover, the surface optical phonon modes of h-BN have energies two times larger than similar modes in SiO<sub>2</sub>, suggesting the possibility of an improved high-temperature and high-electric-field performance of h-BN based graphene devices over those using typical oxide/graphene stacks<sup>23,24</sup>.

To fabricate graphene-on-BN, we used a mechanical transfer process, as outlined in Fig. 1 (see Methods). The h-BN flakes used in this study were exfoliated from ultrapure, h-BN single crystals that were grown by the method described in ref. 25. The optical contrast on 285-nm SiO<sub>2</sub>/Si substrates is sufficient to easily identify h-BN flakes with thicknesses down to a single monolayer (see Fig. 1b and ref. 26). Figure 2 shows AFM images of monolayer graphene transferred onto  $\sim 14$ -nm-thick h-BN (see Supplementary Information). The transferred graphene is free of wrinkles or distortions, consistent with previous reports of similar polymethyl-methacrylate (PMMA)-based transfer techniques<sup>27</sup>. A histogram of the roughness of graphene on h-BN (Fig. 2b) shows it to be indistinguishable from bare h-BN and approximately three times less rough than SiO<sub>2</sub>. We conclude that the graphene membrane conforms to the atomically flat h-BN, consistent with previous reports on both rippled<sup>9</sup> and flat<sup>21</sup> surfaces.

Electronic transport measurements of monolayer graphene transferred onto h-BN indicate that the resulting two-dimensional electronic systems are of high quality. Figure 3a shows the resistance of a typical monolayer graphene sample on h-BN as a function of applied backgate voltage,  $V_g$ . The resistivity peak, corresponding to the overall charge neutrality point, is extremely narrow and occurs at nearly zero gate voltage. The conductivity (dotted line, Fig. 3a inset) is strongly sublinear in carrier density, indicating a crossover from scattering dominated by charge impurities at low densities to short-range impurity scattering at large carrier densities<sup>4–6,11,28</sup>. The data are well fit (solid line in figure) by a self-consistent Boltzmann equation for diffusive transport that includes both long- and short-range scattering<sup>5,6</sup>,  $\sigma^{-1} = (ne\mu_C + \sigma_0)^{-1} + \rho_s$ , where  $\mu_C$  is the density-independent mobility due to charged-impurity Coulomb (long-range) scattering,  $\rho_s$  is the contribution to resistivity from short-range scattering, and  $\sigma_0$  is the residual conductivity at the charge neutrality point. We obtain  $\mu_C \approx 60,000 \text{ cm}^2 \text{ V}^{-1} \text{ s}^{-1}$ , three times larger than that on SiO<sub>2</sub> using a similar analysis<sup>28</sup>, and  $\rho_s \approx 71 \Omega$ , which is similar to values obtained on SiO<sub>2</sub>. This indicates

<sup>1</sup>Department of Electrical Engineering, Columbia University, New York, New York, 10027, USA, <sup>2</sup>Department of Mechanical Engineering, Columbia University, New York, New York, 10027, USA, <sup>3</sup>Department of Physics, Columbia University, New York, New York, 10027, USA, <sup>4</sup>SKKU Advanced Institute of Nanotechnology (SAINT), Sungkyunkwa University, Suwon 440-746, Korea, <sup>5</sup>Department of Mechanical Engineering, Sungkyunkwa University, Suwon 440-746, Korea, <sup>6</sup>Advanced Materials Laboratory, National Institute for Materials Science, 1-1 Namiki, Tsukuba, 305-0044, Japan.

\*e-mail: jh2228@columbia.edu; cdean@cisl.columbia.edu

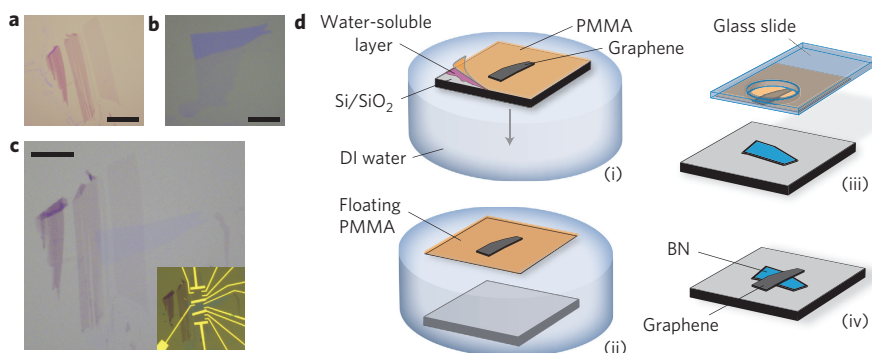


**Figure 1 | Mechanical transfer process.** **a–c**, Optical images of graphene (**a**) and h-BN (**b**) before and after (**c**) transfer. Scale bars, 10  $\mu\text{m}$ . Inset: electrical contacts. **d**, Schematic illustration of the transfer process used to fabricate graphene-on-BN devices (see text for details).

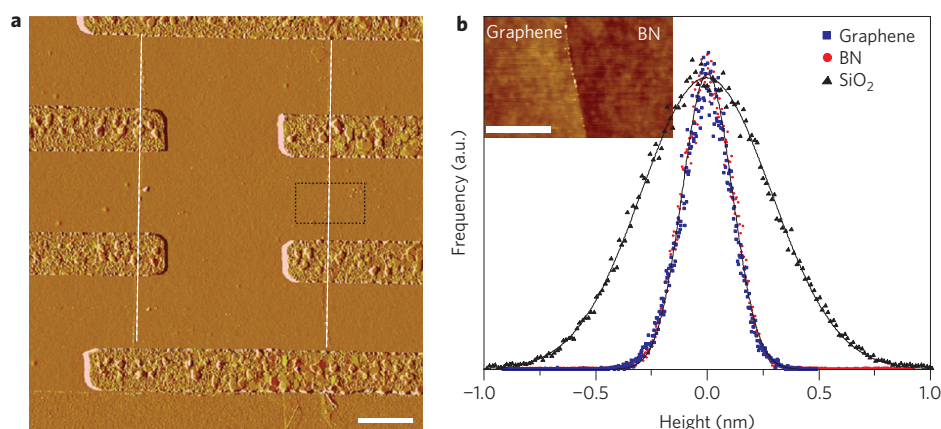


**Figure 2 | Atomic force microscopy.** **a**, AFM image of monolayer graphene on BN with electrical leads. White dashed lines indicate the edge of the graphene flake. Scale bar, 2  $\mu\text{m}$ . **b**, Histogram of the height distribution (surface roughness) measured by AFM for  $\text{SiO}_2$  (black triangles), h-BN (red circles) and graphene-on-BN (blue squares). Solid lines are Gaussian fits to the distribution. Inset: high-resolution AFM image showing a comparison of graphene and BN surfaces, corresponding to the dashed square in **a**. Scale bar, 0.5  $\mu\text{m}$ .

a threefold decrease in the scattering rate due to charge impurities in this sample, but a similar degree of short-range scattering, in comparison to the best  $\text{SiO}_2$  samples. This suggests that the sublinear shape does not result from increased short-range scattering on BN substrates, but rather from a substantially reduced charge impurity contribution, which reveals the effects of short-range scattering at comparatively lower densities. Similar behaviour was observed in more than 10 monolayer graphene samples and, importantly, we always measured a higher mobility for BN-supported graphene when compared to portions of the same flake on the nearby  $\text{SiO}_2$  surface (see Supplementary Information). For the monolayer graphene device shown here, the Hall mobility was  $\sim 25,000 \text{ cm}^2 \text{ V}^{-1} \text{ s}^{-1}$  at high densities, where short-range scattering appears to dominate. Although the origin of short-range scattering remains controversial, the similar values of  $\rho_s$  for  $\text{SiO}_2$ - and h-BN-supported graphene samples suggests that scattering off ripples and out-of-plane vibrations<sup>10,11</sup> may not comprise a significant contribution in our samples, because these are likely to be suppressed on atomically flat h-BN. For comparison with the literature, we note that the field effect mobility, defined by the derivative of the Drude formula,  $\mu_{\text{FE}} = (1/C)d\sigma/dV_g$ , varies from  $\sim 25,000 \text{ cm}^2 \text{ V}^{-1} \text{ s}^{-1}$  at high densities (in agreement with the Hall mobility) to  $\sim 140,000 \text{ cm}^2 \text{ V}^{-1} \text{ s}^{-1}$  near the charge neutrality point.

The width of the resistivity peak at the charge neutrality point gives an estimate of the charge-carrier inhomogeneity resulting from electron–hole puddle formation at low densities<sup>29</sup>. In Fig. 3a

the full-width at half-maximum (FWHM) of  $\rho(V_g)$  is  $\sim 1 \text{ V}$ , giving an upper bound for disorder-induced carrier density fluctuation of  $\delta n < 7 \times 10^{10} \text{ cm}^{-2}$ , a factor of  $\sim 3$  improvement over  $\text{SiO}_2$ -supported samples<sup>12</sup>. An alternative estimate of this inhomogeneity is obtained from the temperature dependence of the minimum conductivity. In Fig. 3c,  $\sigma_{\text{min}}$  increases by a factor of two between 4 K and 200 K. Such a strong temperature dependence has previously only been observed in suspended samples, with substrate-supported samples typically exhibiting  $< 30\%$  variation in the same range<sup>13</sup>.  $\sigma_{\text{min}}$  is expected to vary with temperature only for  $k_B T > E_{\text{puddle}}$ , where for monolayer graphene<sup>13</sup>  $E_{\text{puddle}} \approx \hbar v_f \sqrt{\pi \delta n}$  ( $v_f$  is the Fermi velocity). Here,  $\sigma_{\text{min}}$  saturates to  $\sim 6e^2/h$  for  $T \lesssim 15 \text{ K}$ , giving an upper bound of  $\delta n \approx 1 \times 10^9 \text{ cm}^{-2}$ . The  $\delta n$  estimated by these two measures is consistent with a similar analysis performed on suspended devices<sup>13,30</sup>.

It has been proposed that a bandgap would be induced in graphene aligned to an h-BN substrate<sup>20</sup>. In our experiment the graphene had a random crystallographic orientation to the substrate, and thus we did not expect the necessary sublattice symmetry breaking to occur. Indeed, the temperature dependence of  $\sigma_{\text{min}}$  observed here does not follow the simply activated behaviour that would be indicative of an energy gap. Although we cannot rule out the possibility of locally gapped regions resulting from symmetry breaking over finite length scales, we see no evidence from transport measurements that an appreciable gap is present in this randomly stacked graphene on h-BN.

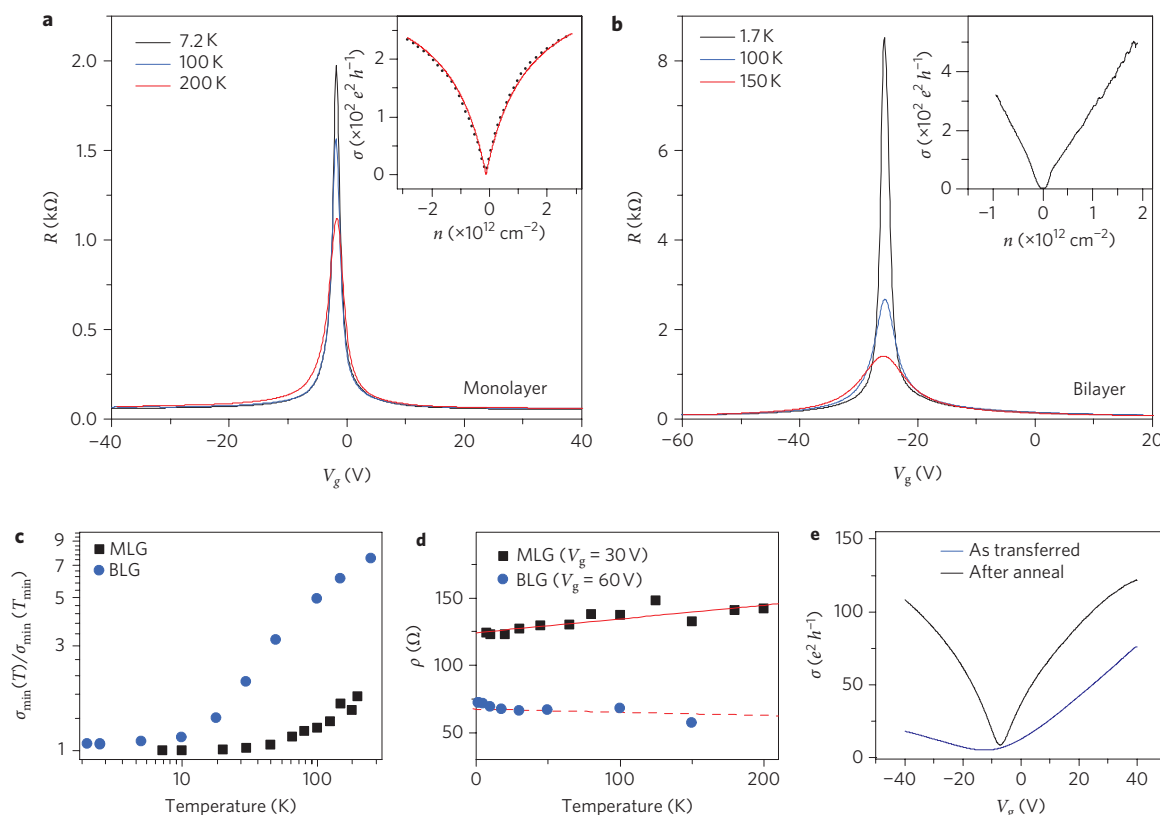


**Figure 3 | Transport properties.** **a,b**, Resistance versus applied gate voltage for monolayer graphene (**a**) and bilayer graphene (**b**) on h-BN. Insets: corresponding conductivity. **c,d**, Temperature dependence of the conductivity minimum (**c**) and high-density resistivity (**d**) for both devices. Solid and dashed lines in **d** are linear fits to the data. MLG, monolayer graphene; BLG, bilayer graphene. **e**, Conductivity of a different monolayer graphene sample comparing the room-temperature transport characteristics measured for as-transferred-to-h-BN (blue curve) and after annealing in  $H_2$ /Ar (black curve).

Transport measurements from bilayer graphene transferred to h-BN are shown in Fig. 3b. The corresponding conductivity is linear with gate voltage up to large densities, as expected for bilayer graphene in the presence of long- and short-range scalar potential disorder<sup>31</sup>. The (density-independent) electron and hole Hall mobilities are  $\sim 60,000 \text{ cm}^{-2} \text{ V}^{-1} \text{ s}^{-1}$  and  $\sim 80,000 \text{ cm}^{-2} \text{ V}^{-1} \text{ s}^{-1}$ , respectively, at  $T = 2 \text{ K}$ , with a value of  $40,000 \text{ cm}^{-2} \text{ V}^{-1} \text{ s}^{-1}$  measured at room temperature in air for this same device. The FWHM of the resistivity peak is  $\sim 1.2 \text{ V}$ , giving an estimate of the carrier inhomogeneity density of  $\delta n \approx 9 \times 10^{10} \text{ cm}^{-2}$ . Both the mobility and inhomogeneity are comparable to the best reported suspended bilayer graphene devices<sup>30</sup> and almost an order of magnitude better than bilayer graphene on  $\text{SiO}_2$ <sup>11</sup>. The temperature dependence of  $\sigma_{\min}$  (blue circles in Fig. 3c) is much stronger than in monolayer graphene, consistent with previous studies<sup>11,30</sup>. (We note that the bilayer graphene studied here, although undoped immediately after sample fabrication and annealing, was contaminated upon insertion into a helium flow cryostat; thereafter the charge neutrality point was found at  $V_g \approx -27 \text{ V}$ . The temperature dependence at the charge neutrality point may therefore be due in part to an electric field induced energy gap<sup>32,33</sup>.)

The temperature dependence of the resistivity at high densities for both monolayer graphene and bilayer graphene is shown in Fig. 3d. Monolayer graphene resistance increases linearly with temperature (solid line in Fig. 3d) due to longitudinal acoustic phonon scattering,  $\rho_{\text{LA}}(T) = (h/e^2)[(\pi^2 D_A^2 k_B T)/(2h^2 \rho_s v_s^2 v_f^2)]$ , where  $\rho_s = 7.6 \times 10^{-7} \text{ kg m}^{-2}$  is the graphene mass density,  $v_f = 1 \times 10^6 \text{ m s}^{-1}$  is the Fermi velocity,  $v_s = 2 \times 10^4 \text{ m s}^{-1}$  is the longitudinal acoustic phonon velocity and  $D_A$  is the acoustic deformation potential<sup>8,13</sup>. Linear fits to the electron (hole) branches give  $D_A \approx 18 \text{ eV}$  ( $D_A \approx 21 \text{ eV}$ ). In contrast, bilayer graphene exhibits a very

weak temperature dependence, with a slightly negative overall trend (dashed line in Fig. 3d). Both findings agree with previous measurements<sup>8,11,13,28</sup>. We note that no indication of activated remote surface phonon scattering is seen in monolayer graphene (bilayer graphene) up to 200 K (240 K). However, further studies in a variable-temperature ultra-high vacuum (UHV) environment<sup>8</sup> are required to explore the high-temperature behaviour in graphene-on-BN more fully.

The chemical reactivity of our graphene-on-h-BN heterostructures appears to be markedly different from that of graphene-on- $\text{SiO}_2$ . Figure 3e shows the room-temperature conductivity of a typical monolayer graphene layer before and after annealing in a  $H_2$ /Ar flow at  $340^\circ \text{C}$  for 3.5 h (see Methods). Annealing substantially enhances the carrier mobility while leaving the position of the charge neutrality point virtually unchanged. The low mobility immediately post-transfer may be due to neutral transfer residues and/or local strains that are relaxed upon heating. The lack of doping after heating in  $H_2$ /Ar is in stark contrast to  $\text{SiO}_2$ -supported devices, where heat treatment typically results in heavy doping of the graphene, often more than  $5 \times 10^{12} \text{ cm}^{-2}$ , after re-exposure to air. The mechanism responsible for this different behaviour remains unclear, because features of both the substrate (for example, surface chemistry) and the graphene (for example, roughness) may play a role.

Magnetotransport measurements provide further confirmation of the high material quality achieved in these samples. Figure 4a shows the magnetoresistance  $R_{xx}$  and Hall conductivity  $\sigma_{xy}$  as a function of density at  $B = 14 \text{ T}$  for monolayer graphene, derived from simultaneous measurement of magnetoresistance  $R_{xx}$  and Hall resistance  $R_{xy}$  in the Hall bar geometry shown in Fig. 1. Complete lifting of the fourfold degeneracy<sup>34</sup> of the zero-energy



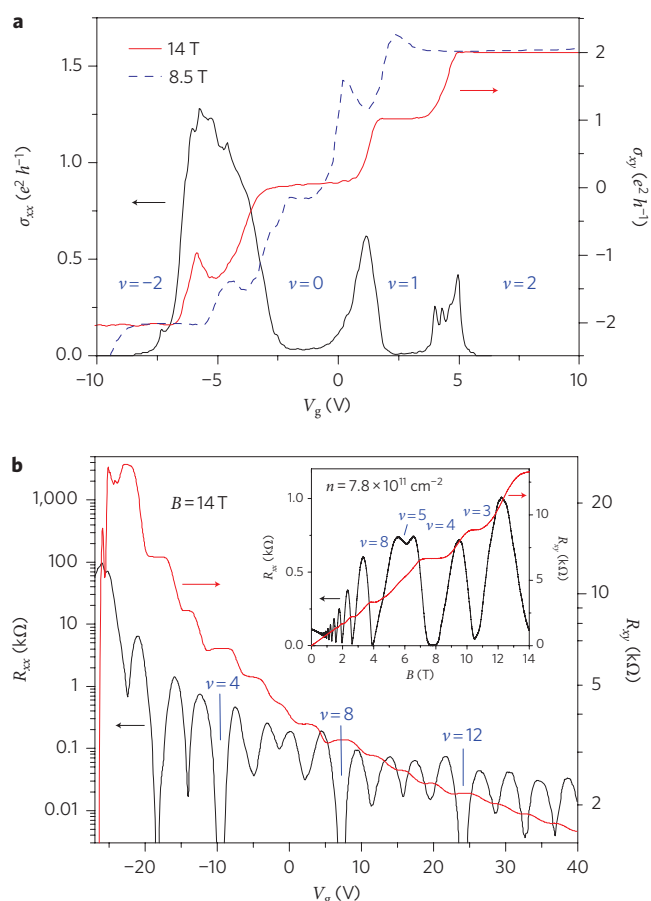


**Figure 4 | Magnetotransport.** **a**, Longitudinal (left axis) and Hall conductivity (right axis) versus gate voltage at  $B = 14$  T (solid line) and 8.5 T (dashed line) for monolayer graphene. **b**, Longitudinal (left axis) and Hall (right axis) resistance versus gate voltage at  $B = 14$  T for bilayer graphene. Inset: magnetic field sweep at fixed density. Shubnikov-de Haas oscillations begin at  $\sim 0.4$  T with Landau level symmetry breaking appearing at fields less than 6 T. ( $T \approx 2$  K in both panels).

Landau level is observed, with the additional quantum Hall states at  $\nu = 0, +1, \pm 2$  exhibiting quantized Hall conductance  $\sigma_{xy} = \nu e^2/h$ , together with vanishing  $\sigma_{xx}$ . The dashed line in Fig. 4a indicates that signatures of the  $\nu = \pm 1$  quantum Hall effect are visible at fields as low as  $B = 8.5$  T, more than a factor of two smaller than reported for monolayer graphene on  $\text{SiO}_2$ <sup>34</sup>.

A complete sequence of broken-symmetry Landau levels is visible in bilayer graphene at  $B = 14$  T (Fig. 4b). In our device, the substrate-supported geometry allowed us to probe much higher densities than is possible in suspended devices of similar quality<sup>30</sup>. Quantized Hall resistance is observed at  $R_{xy} = (1/\nu)(h/e^2)$ , concomitant with minima in  $R_{xx}$  for all integer filling factors from  $\nu = 1$  to at least  $\nu = 16$ . Density sweeps at lower fields (see Supplementary Information) show that the lifting of the expected fourfold degeneracy in bilayer graphene<sup>30</sup> is observable up to at least the fifth Landau level at less than 5 T. Complete quantization of the fourfold degenerate Landau levels and Shubnikov-de Haas oscillations is seen down to 2 and 0.4 T, respectively (inset, Fig. 4b; see also Supplementary Information).

In the lowest Landau level the even-integer,  $\nu = 2$ , quantum Hall state has a larger gap compared to the odd-integer states,  $\nu = 1$  and 3, as judged by the depth of the  $R_{xx}$  minimum<sup>30,35</sup>. Interestingly, in the second Landau level, the situation is reversed, with the even integer state ( $\nu = 6$ ) weaker than the odd integers ( $\nu = 5, 7$ ). A

full understanding of symmetry breaking with increasing Landau level index is complicated by the fact that the applied gate voltage (and also residual extrinsic doping) breaks the layer degeneracy through the resultant electric field while simultaneously modifying the exchange energy by modulation of the carrier density. Analysis of this trend is, therefore, left to a future study in dual-gated devices where the transverse electric field can be tuned independently. Preservation of high mobility in dual-gated devices may be achieved by fabricating h-BN-graphene-h-BN stacks using a two-transfer technique<sup>22</sup>.

## Methods

Graphene-on-BN devices were fabricated according to the procedure illustrated in Fig. 1d. Fabrication began with the mechanical exfoliation of h-BN single crystals onto silicon wafers coated in 285-nm thermal oxide (Fig. 1d(i)). Graphene was exfoliated separately onto a polymer stack consisting of a water-soluble layer (Mitsubishi Rayon aquaSAVE) and PMMA, and the substrate was floated on the surface of a deionized water bath. The PMMA thickness was precisely tuned to allow identification of monolayer graphene by optical means. The graphene layer thickness was then verified by Raman spectroscopy before transfer. Once the water-soluble polymer had dissolved, the Si substrate sank to the bottom of the bath (Fig. 1d(ii)), leaving the extremely hydrophobic PMMA floating on top. The PMMA membrane was adhered to a glass transfer slide (Fig. 1d(iii)), which was clamped onto the arm of a micromanipulator mounted on an optical microscope. Using the microscope to optically locate the position of the graphene flake on the suspended polymer film, the graphene was precisely aligned to the target BN and the two brought into contact. With this technique, the graphene could be positioned to within a few micrometres of the target position. During transfer, the target substrate was heated to 110 °C in an effort to drive off any water adsorbed on the surface of the graphene or h-BN flakes, as well as to promote good adhesion of the PMMA to the target substrate. Once transferred, the PMMA was dissolved in acetone (Fig. 1d(iv)). Electrical leads were deposited using standard electron beam lithography, after which all samples were annealed in flowing  $\text{H}_2/\text{Ar}$  gas at 340 °C for 3.5 h to remove resist residues. The devices presented in the main text did not undergo any further treatment (such as *in situ* vacuum annealing) after removal from the  $\text{H}_2/\text{Ar}$  flow.

AFM images were acquired in air using silicon cantilevers operated in tapping mode. Surface roughness was reported as the standard deviation of the surface height distribution (determined by a fitted Gaussian), measured on an area of  $0.3 \mu\text{m}^2$ . Transport measurements were acquired in a four-terminal geometry using standard lock-in techniques at  $\sim 17$  Hz. Samples were cooled in a variable-temperature ( $\sim 2$ –300 K) liquid  $^4\text{He}$  flow cryostat with the sample in vapour.

Received 27 May 2010; accepted 22 July 2010;  
published online 22 August 2010

## References

- Geim, A. & Novoselov, K. The rise of graphene. *Nature Mater.* **6**, 183–191 (2007).
- Neto, A., Guinea, F., Peres, N. M. R., Novoselov, K. S. & Geim, A. K. The electronic properties of graphene. *Rev. Mod. Phys.* **81**, 109–162 (2009).
- Ando, T. Screening effect and impurity scattering in monolayer graphene. *J. Phys. Soc. Jpn* **75**, 074716 (2006).
- Nomura, K. & MacDonald, A. H. Quantum transport of massless Dirac fermions. *Phys. Rev. Lett.* **98**, 076602 (2007).
- Hwang, E. H., Adam, S. & Das Sarma, S. Carrier transport in two-dimensional graphene layers. *Phys. Rev. Lett.* **98**, 186806 (2007).
- Hwang, E. H., Adam, S. & Das Sarma, S. Carrier transport in two-dimensional graphene layers. *Phys. Rev. Lett.* **98**, 18392–18397 (2007).
- Fratini, S. & Guinea, F. Substrate-limited electron dynamics in graphene. *Phys. Rev. B* **77**, 195415 (2008).
- Chen, J.-H., Jang, C., Xiao, S., Ishigami, M. & Fuhrer, M. S. Intrinsic and extrinsic performance limits of graphene devices on  $\text{SiO}_2$ . *Nature Nanotech.* **3**, 206–209 (2008).
- Ishigami, M., Chen, J. H., Cullen, W. G., Fuhrer, M. S. & Williams, E. D. Atomic structure of graphene on  $\text{SiO}_2$ . *Nano Lett.* **7**, 1643–1648 (2007).
- Katsnelson, M. I. & Geim, A. K. Electron scattering on microscopic corrugations in graphene. *Phil. Trans. R. Soc. A* **366**, 195–204 (2007).
- Morozov, S. V. *et al.* Giant intrinsic carrier mobilities in graphene and its bilayer. *Phys. Rev. Lett.* **100**, 016602 (2008).
- Martin, J. *et al.* Observation of electron-hole puddles in graphene using a scanning single-electron transistor. *Nature Phys.* **4**, 144–148 (2008).
- Bolotin, K. I., Sikes, K. J., Hone, J., Stormer, H. L. & Kim, P. Temperature-dependent transport in suspended graphene. *Phys. Rev. Lett.* **101**, 096802 (2008).
- Du, X., Skachko, I., Barker, A. & Andrei, E. Y. Approaching ballistic transport in suspended graphene. *Nature Nanotech.* **3**, 491–495 (2008).

15. Hong, X. *et al.* High-mobility few-layer graphene field effect transistors fabricated on epitaxial ferroelectric gate oxides. *Phys. Rev. Lett.* **102**, 136808 (2009).
16. Ponomarenko, L. A. *et al.* Effect of a high-kappa environment on charge carrier mobility in graphene. *Phys. Rev. Lett.* **102**, 206603 (2009).
17. Lafkioti, M. *et al.* Graphene on a hydrophobic substrate: doping reduction and hysteresis suppression under ambient conditions. *Nano Lett.* **10**, 1149–1153 (2010).
18. Liao, L., Bai, J., Qu, Y., Huang, Y. & Duan, X. Single-layer graphene on Al<sub>2</sub>O<sub>3</sub>/Si substrate: better contrast and higher performance of graphene transistors. *Nanotechnology* **21**, 015705 (2010).
19. Watanabe, K., Taniguchi, T. & Kanda, H. Direct-bandgap properties and evidence for ultraviolet lasing of hexagonal boron nitride single crystal. *Nature Mater.* **3**, 404–409 (2004).
20. Giovannetti, G., Khomyakov, P., Brocks, G., Kelly, P. & Brink, J. V. D. Substrate-induced band gap in graphene on hexagonal boron nitride: *ab initio* density functional calculations. *Phys. Rev. B* **76**, 073103 (2007).
21. Lui, C. H., Liu, L., Mak, K. F., Flynn, G. W. & Heinz, T. F. Ultraflat graphene. *Nature* **462**, 339–341 (2009).
22. Young, A. F. *et al.* Electronic compressibility of gapped bilayer graphene. preprint at arXiv:1004.5556v2 (2010).
23. Meric, I. *et al.* Current saturation in zero-bandgap, top-gated graphene field-effect transistors. *Nature Nanotech.* **3**, 654–659 (2008).
24. Schwierz, F. Graphene transistors. *Nature Nanotech.* **5**, 487–496 (2010).
25. Taniguchi, T. & Watanabe, K. Synthesis of high-purity boron nitride single crystals under high pressure by using Ba–Bn solvent. *J. Cryst. Growth* **303**, 525–529 (2007).
26. Lee, C. *et al.* Frictional characteristics of atomically thin sheets. *Science* **328**, 76–80 (2010).
27. Reina, A. *et al.* Large area, few-layer graphene films on arbitrary substrates by chemical vapor deposition. *Nano Lett.* **9**, 30–35 (2009).
28. Hong, X., Zou, K. & Zhu, J. The quantum scattering time and its implications on scattering sources in graphene. *Phys. Rev. B* **80**, 241415 (2009).
29. Bolotin, K. I. *et al.* Ultrahigh electron mobility in suspended graphene. *Solid State Commun.* **146**, 351–355 (2008).
30. Feldman, B. E., Martin, J. & Yacoby, A. Broken-symmetry states and divergent resistance in suspended bilayer graphene. *Nature Phys.* **5**, 889–893 (2009).
31. Adam, S. & Sarma, S. D. Boltzmann transport and residual conductivity in bilayer graphene. *Phys. Rev. B* **77**, 115436 (2007).
32. McCann, E. Asymmetry gap in the electronic band structure of bilayer graphene. *Phys. Rev. B* **74**, 161403 (2006).
33. Castro, E. V. *et al.* Biased bilayer graphene: semiconductor with a gap tunable by the electric field effect. *Phys. Rev. Lett.* **99**, 216802 (2007).
34. Zhang, Y. *et al.* Landau-level splitting in graphene in high magnetic fields. *Phys. Rev. Lett.* **96**, 136806 (2006).
35. Zhao, Y. *et al.* Symmetry breaking in the zero-energy Landau level in bilayer graphene. *Phys. Rev. Lett.* **104**, 066801 (2010).

### Acknowledgements

The authors thank D. Sukhdeo and N. Bakhtskaya for help with device fabrication. This work is supported by the Defense Advanced Research Projects Agency (Carbon Electronics for RF Applications), Air Force Office of Scientific Research, Office of Naval Research, Semiconductor Research Corporation Focus Center Research Program, The National Science Foundation (CHE-0117752), New York State Foundation for Science, and Technology and Innovation (NYSTAR).

### Author contributions

C.R.D. and A.F.Y. performed the experiments, including sample fabrication, measurement, characterization and development of the transfer technique. I.M. contributed to sample fabrication, measurement and development of the transfer technique. C.L. and W.L. contributed to sample fabrication. S.S. contributed to development of the transfer technique. K.W. and T.T. synthesized the h-BN samples. P.K., K.L.S., and J.H. provided advice on the experiments.

### Additional information

The authors declare no competing financial interests. Supplementary information accompanies this paper at [www.nature.com/naturenanotechnology](http://www.nature.com/naturenanotechnology). Reprints and permission information is available online at <http://npg.nature.com/reprintsandpermissions/>. Correspondence and requests for materials should be addressed to C.R.D. and J.H.